PROCEEDINGS OF SPIE

SPIEDigitalLibrary.org/conference-proceedings-of-spie

Optical simulations for the Wolter-I collimator in the VERT-X calibration facility

Spiga, D., Moretti, A., Pareschi, G., Sironi, G., Bavdaz, M., et al.

D. Spiga, A. Moretti, G. Pareschi, G. Sironi, M. Bavdaz, I. Ferreira, G. Valsecchi, F. Marioni, F. Zocchi, "Optical simulations for the Wolter-I collimator in the VERT-X calibration facility," Proc. SPIE 11822, Optics for EUV, X-Ray, and Gamma-Ray Astronomy X, 118220L (14 September 2021); doi: 10.1117/12.2589835

SPIE.

Event: SPIE Optical Engineering + Applications, 2021, San Diego, California, United States

Optical simulations for the Wolter-I collimator in the VERT-X calibration facility

D. Spiga*, A. Moretti, G. Pareschi, G. Sironi
INAF-Osservatorio Astronomico di Brera, Via E. Bianchi 46, 23807 Merate (Italy)

M. Bavdaz, I. Ferreira
European Space Agency, Keplerlaan 1, 2201 AZ Noordwijk (Netherlands)

G. Valsecchi, F. Marioni, F. Zocchi
Media Lario Srl, via al Pascolo, 23842 Bosisio Parini (Italy)

ABSTRACT

The VERT-X X-ray calibration facility, currently in prototypal realization phase supported by ESA, will be a vertical X-ray beamline able to test and calibrate the entire optical assembly of the ATHENA X-ray telescope. Owing to its long focal length (12 m), a full-illumination test of the entire focusing system would require a parallel and uniform X-ray beam as large as the optical assembly itself (2.5 m). Moreover, the module should better be laid parallel to the ground in order to minimize the effects of gravity deformations. Therefore, the ideal calibration facility would consist of a vertical beam, with the source placed at very large distance (>> 500 m) under high vacuum (10^{-6} mbar). Since such calibration systems do not exist, and also appear to be very hard to manufacture, VERT-X will be based on a different concept, i.e., the raster scan of a tightly (≈ 1 arcsec) collimated X-ray beam, generated by a microfocus source and made parallel via a precisely shaped Wolter-I mirror. In this design, the mirror will be made of two segments (paraboloid + hyperboloid) that, for the X-ray beam collimation to be preserved, will have to be accurately finished and maintain their mutual alignment to high accuracy during the scan. In this paper, we show simulations of the reflected wavefront based on physical optics and the expected final imaging quality, for different polishing levels and misalignments for the two segments of the VERT-X collimator.

Keywords: ATHENA, VERT-X, Wolter-I, roughness, wave optics

1. THE VERT-X CALIBRATION FACILITY FOR ATHENA

The ATHENA (Advanced Telescope for High-ENergy Astrophysics) X-ray telescope is the second large mission selected by ESA within the Cosmic Vision Program, with launch scheduled in the early 2030s.[1] It will be the largest X-ray telescope ever built, with a 2.5 m diameter, a 1.4 m^2 effective area at 1 keV, and an angular resolution of 5 arcsec half-energy width (HEW). This large focusing system requires a completely different approach to X-ray mirror manufacturing: the focusing module of ATHENA will be populated with MMs (*mirror modules*), based on the *silicon pore optics* (SPO) technology, conceived and developed by ESA and the *Cosine* company (Warmond, The Netherlands), where SPO MMs will be manufactured in series.[2] Manufacturing a large number (> 600) of focusing building blocks then implies the problem of aligning and integrating all the modules confocally: this delicate task can be effectively accomplished in an optical bench, e.g. under parallel UV light, having all the centroids of the MM's focal spots converge to the same point. To this specific purpose, a dedicated alignment and integration facility is being built at Media Lario.[3]

However, testing and calibrating the complete ATHENA *mirror assembly* (MA) in X-rays is a different story. Not only it needs a large, high vacuum enclosure for housing the ATHENA optics and 12 m of its focal length: it also requires a highly collimated (e.g., nearly parallel) X-ray beam to simulate the incidence from a source at virtually infinite distance. While collimating UV light with large high-quality paraboloidal mirrors is quite easy, as it can be done in normal incidence, this is much more complicated in X-rays by the grazing incidence at a shallow angle α that reduces the beam area, with respect to that of the mirror, by a factor of $\tan\alpha$. For this reason, low-divergence and

* corresponding author: daniele.spiga@inaf.it, phone +39-0272320-427

Optics for EUV, X-Ray, and Gamma-Ray Astronomy X, edited by Stephen L. O'Dell, Jessica A. Gaskin, Giovanni Pareschi, Proc. of SPIE Vol. 11822, 118220L · © 2021 SPIE · CCC code: 0277-786X/21/$21 · doi: 10.1117/12.2589835

broad beams have so far been obtained locating the source at very large distance, such as PANTER at MPE (125 m),[4] or the XRCF beamline at MSFC (500 m). Nevertheless, the long focal length of ATHENA, the dimensions of the mirror assembly, and the narrow *point spread function* (PSF) to be measured would require a consistent upgrade to these facilities, not only in order to accommodate the entire optic, but also to minimize the aberrations resulting from the finiteness of the source distance. Finally, PANTER and XRCF are horizontal beamlines; hence, the MA would suffer from significant gravity deformation during tests, which would be completely absent on orbit.

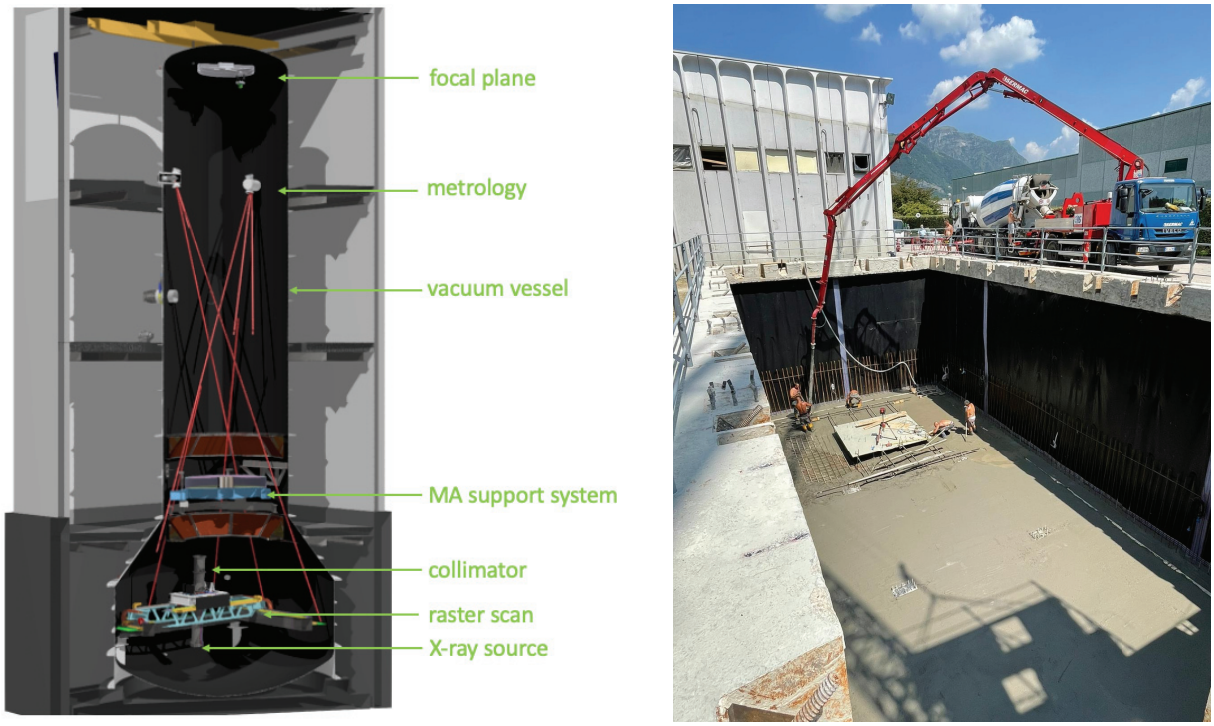

Figure 1. Left: a schematic of the VERT-X facility in its current design. The mirror assembly (MA) is laid horizontal and a parallel X-ray beam is scanned throughout its aperture. The integrated PSF is recorded on the focal plane. Right: excavation in progress at Media Lario for the ATHENA MA alignment and integration facility. VERT-X will be built next to it.

All these motivations suggested us the concept of the VERT-X calibration facility.[5] Rather than aiming at the generation of a parallel beam as broad as the full MA aperture, VERT-X is based on the raster scan concept of a small, highly collimated and parallel (HEW ≈ 1 arcsec) X-ray beam. During the scan, only a small number of SPO MMs are illuminated at a time and generate a PSF on the focal plane, at a 12 m distance. The beam sweeps the entire ATHENA MA, while the detector collects the focused photons. If the beam maintains its properties, without changing its pointing along the scan duration, the integrated image on the detector will return the full PSF of the ATHENA MA. Properly normalizing the PSF will also yield an absolute measurement of the effective area, mimicking the effect of an astronomical X-ray source. Since the source takes a compact space, all the vacuum tank enclosing the range from source to focal plane (approx. 20 m) can be placed vertically, which in turn allows laying horizontal the ATHENA MA, thereby minimizing gravity deformations. A concept design of VERT-X is illustrated in Figure 1, left. The current planning foresees its construction next to the ATHENA MA alignment and integration facility at Media Lario (Figure 1, right). This choice would also offer additional advantages: 1) complementing the UV facility with an X-ray facility operated in parallel, 2) enable testing the MA in X-rays as the alignment under UV light progresses.

The VERT-X project is financed by ESA and, at the current stage, aiming at the development of the most critical components as defined in the project phase: the raster scan system, the X-ray source, the collimating mirror, and their interfaces.[6] In this paper, we focus on the design and the performance simulation of the X-ray collimating mirror. In Sect. 2, we briefly discuss its Wolter-I design. Sect. 3 reports a preliminary study on manufacturing tolerances, such as roughness and surface errors. Doing this, we have been dealing with 1D simulations based on the Fresnel diffraction formalism,[7] in order to account for aperture diffraction, figure errors, and microroughness at the same time,[8] with some adaption due to the short source-to-mirror distance. The Wolter-I mirror will be manufactured by figuring the two segments (parabolic and hyperbolic) separately, also taking advantage of the experience gained in the production

of the BEaTriX[9] paraboloidal collimator.[10] It is important to ascertain to which accuracy the two segments should be aligned to avoid aberrations in the focusing/collimating properties. In Sect. 4, we show some simulation of the aberrations expected from various misalignment between the two segments of the Wolter-I mirror, using a simple 2D diffraction model,[11] already used for simulating diffractive effects in SPO mirror modules in the context of the SIMPOSIuM project.[12]

2. THE WOLTER-I COLLIMATOR

For the fabrication of the X-ray collimator, we have selected a Wolter-I profile because it suffers much less from aberrations, i.e. wavefront distortions, when the X-ray source is slightly off-axis, compared to a parabolic mirror yielding a parallel beam with the same size.[5] In designing the mirror (Figure 2), we aimed at keeping its dimensions compact enough to be easily scanned in front of the MA aperture, but at the same time returning a collimated beam not too small so to avoid increasing the total scan time. Due to the achievable shape and size of the X-ray source (a customized FAAST by *Sigray*, Concord, California), which can reach a minimum electron spot with gaussian profile and an 8-10 µm FWHM, a residual divergence of 1 arcsec means a focal length of about 2 m or longer. The mirror parameters are listed hereafter.

- Focal length, $f = 2315$ mm
- sagittal RoC at the *intersection plane* (I.P.), $R_0 = 63.04$ mm
- parabolic segment length along axis, $L_1 = 567.45$ mm
- hyperbolic segment length along axis, $L_2 = 515.76$ mm
- incidence angle at the I.P.: $\alpha_1 = 0.42$ deg, $\alpha_2 = 0.36$ deg
- incidence angle ratio at I.P.: $\xi = \alpha_{0P}/\alpha_{0H} = 1.169$
- incidence angle at the parabolic end, $z = + L_1$: $\alpha_1 = 0.39$ deg
- incidence angle at the hyperbolic end, $z = - L_2$: $\alpha_2 = 0.43$ deg

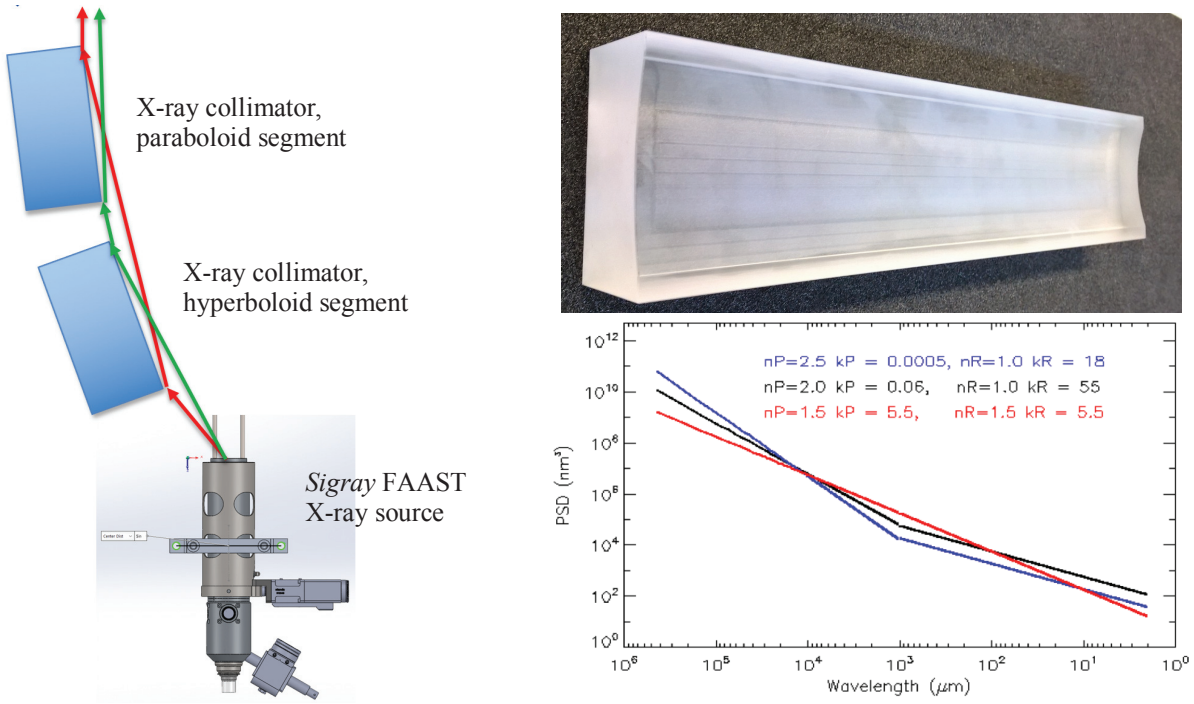

Figure 2. Left: optical sketch of the Wolter-I collimated X-ray source in VERT-X. A microfocus X-ray source (8 µm) in the focus of a Wolter-I grazing incidence mirror generates a parallel X-ray beam. The system works likewise the BEaTriX mirror (top-right), which is a single paraboloid segment. Some possible finishing tolerances of the Wolter-I mirror are shown in terms of power spectral density (PSD, bottom-right).

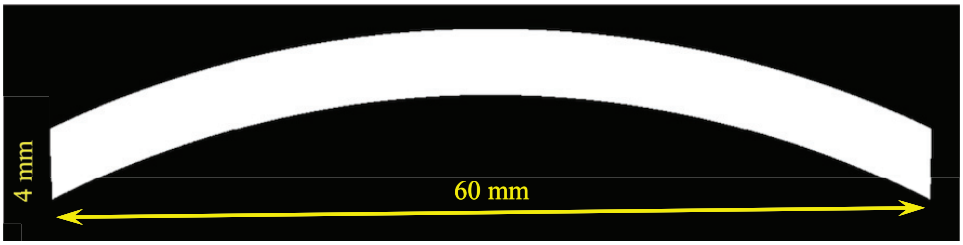

Figure 3: the collimating mirror of VERT-X, seen in projection on-axis. This would also be the shape of the collimated X-ray beam for scanning the ATHENA MA aperture. The arc dimensions are shown in the picture.

The resulting profile exhibits some peculiarities:

1) Unlike X-ray mirrors used in astronomy (such as those of ATHENA), the collimating mirror has been selected with a length that is non-negligible when compared to the focal length. The motivation is in the need to increase the radial beam dimension (Figure 3). However, this requires a parabolic segment *longer* than the hyperbolic one, because of the increased reflection angle at the hyperbolic end.
2) In order to make the parabola and the hyperbola with similar lengths and the *average* incidence angles equal on the two surfaces, the angles at the parabola-hyperbola I.P. have been selected with different values (in the ratio of ξ).
3) Due to the non-negligible L/f ratio, the incidence angles sensitively vary along the mirror length, and so does the high-energy reflectivity. The resulting beam inhomogeneity is anyway small and averaged out by the scan.

These points will later entail some modification of the usual wavefront propagation code, because some approximations usually adopted are no longer valid (Sect. 3). In the perspective of the VERT-X mirror realization, the level of figuring and polishing required to return a residual divergence near 1 arcsec will be definitely challenging. Fortunately, we have matured a considerable experience in the realization of the BEaTriX mirror, which is similar in shape, size, material, and surface roughness tolerances (Figure 2, right) to that of VERT-X. For more information on this specific topic, you can refer to a dedicated SPIE paper.[10]

3. ROUGHNESS TOLERANCES: 1D SIMULATIONS

3.1. Theoretical background

We now come to simulating the PSF of the VERT-X mirror, assuming different possible levels of surface finishing, i.e., the PSDs in Figure 2. In principle, the usual formulae for double reflection mirrors might be used,[7] going backwards: the hyperbolic profile diffracts the electric field from the diverging source to the parabolic profile, then the parabolic profile diffracts it to the observation plane. We might so write the 1D diffraction formula for the diffracted field, E_1, on the parabola:[8]

$$E_1(z_1) = \frac{1}{\sqrt{x_1 \lambda}} \int_{f-L_2}^{f} \sqrt{\frac{x_2}{d_1}} e^{-\frac{2\pi i}{\lambda}(d_1+d_2)} \sin\alpha \, \mathrm{d}z_2 \,, \tag{1}$$

where (Figure 4) d_2 is the source-to-hyperbola distance and where d_1 is the parabola-to-hyperbola distance, clearly as a function of the axial coordinates z_1, z_2 (both with origin in the focal plane) of the parabola and the hyperbola; x_1 and x_2 represent the respective radial coordinates. Nevertheless, Eq. 1 assumes uniform illumination of the hyperbola surface. This condition is usually fulfilled in mirrors used in X-ray astronomy, but not this time. In this peculiar mirror, the distance from the source to hyperbola sensitively varies throughout its length, because f is comparable to L_2. This makes the wavefront intensity uniform *at the hyperbola entrance*, *but not on its surface*. Therefore, Eq. 1 has to be modified as follows:

$$E_1(z_1) = \frac{1}{\sqrt{x_1 \lambda}} \int_{f-L_2}^{f} \sqrt{\frac{x_2}{d_1}} e^{-\frac{2\pi i}{\lambda}(d_1+d_2)} \frac{f}{d_2} q_{12} \, \mathrm{d}z_2 \,. \tag{2}$$

In Eq. 2, we have inserted the additional factor f/d_2 to count the field amplitude decrease in inverse proportion to the distance from the source. Neither can the variation of the *obliquity factor* q_{12} be neglected. When the mirror is very

short compared to the focal length, it can be approximated with the constant sinα without compromising the results significantly. For the VERT-X collimator, the incidence angle change makes the obliquity factors variable and sensitively different from sinα. For the first diffraction, the obliquity factor can be written as follows:

$$q_{12}(z_1) = \frac{\cos \widehat{d_1 n_H} - \cos \widehat{d_2 n_H}}{2}, \tag{3}$$

where the cosine arguments are the angles between the oriented distances $\underline{d}_1$, $\underline{d}_2$, and the local normal $\underline{n}_H$ to the hyperbolic profile. Numerical integration of Eq. 2 at 0.2 keV correctly returns (Figure 5, left) a uniform illumination on the parabola, superimposed to diffraction fringes near the illumination edge. In practice, these fringes are hardly observable when the spatial and temporal incoherence (finite extent and polychromatic spectrum) of the X-ray source is accounted for in the computation.

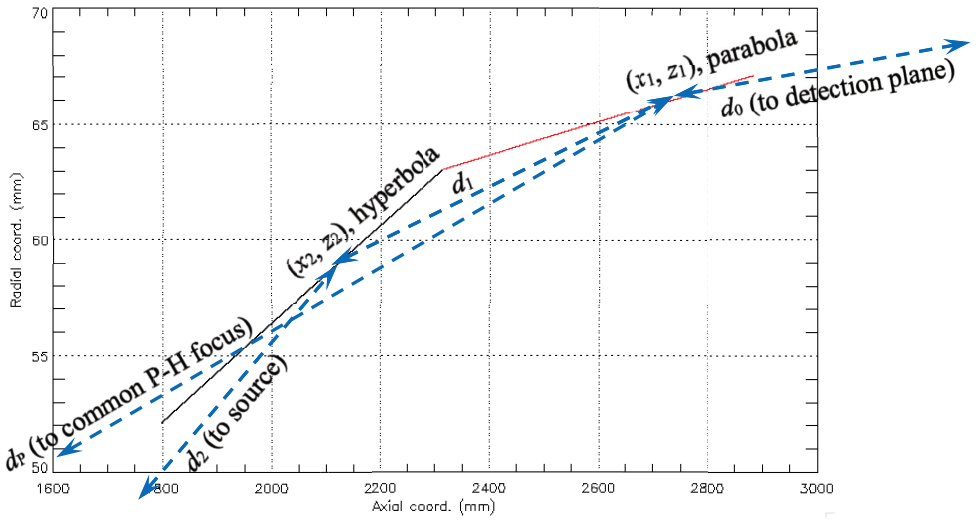

Figure 4: geometry for wavefront diffraction in the Wolter-I mirror used as collimator. The parabola-hyperbola intersection plane is located 2315 mm away from the source.

As for the second diffraction, the field amplitude and phase on the parabola are now enclosed in the $E_1(z_1)$ term, but the obliquity factor q_{01} has, again, to be accounted for in the integration:

$$E_0(x_0) = \frac{1}{\sqrt{x_0 \lambda}} \int_f^{f+L_1} E_1(z_1) \sqrt{\frac{x_1}{d_0}} e^{-\frac{2\pi i}{\lambda} d_0} q_{01} \, \mathrm{d}z_1, \tag{4}$$

where d_1 has the same meaning as in Eq. 1, and d_0 represents the generic distance from the parabola to the point of the reference wavefront (x_0, z_0), where it is supposed to impinge on the MA location under test (z_0 is fixed, 2.5 m beyond the mirror end, the exact value is irrelevant). The obliquity factor q_{01} has an expression similar to Eq. 3:

$$q_{12}(z_1) = \frac{\cos \widehat{d_0 n_P} - \cos \widehat{d_P n_P}}{2}, \tag{5}$$

excepting $\underline{n}_P$ that is, this time, the normal to the parabolic profile and the direction of $\underline{d}_P$ has been taken from the common (outer) parabola-hyperbola focus (Figure 4). The result of the computation at 0.2 keV, displayed in Figure 5, right, returns a uniform wavefront within a 4 mm width, as expected. In this case also, diffraction fringes will likely be unobservable due to the lack of coherence for the X-ray source in use (as opposite to a coherent source, e.g. a Free Electron Laser; in this case, the coherent superposition from different points of the source would reproduce a gaussian profile).[13]

The obtained wavefront is uniform in intensity, but this does not tell anything about the most important aspect, i.e., the *planarity* of the wavefront. This might be assessed, e.g., having the wavefront impinge onto a parabolic mirror and inspecting the resulting PSF. The easiest and fastest way to simulate this re-focusing process is to take the square module of the Fourier transform (FT) of the collimated wavefront in Figure 5, right. Doing so returns, in the case of a perfect Wolter-I collimator, the red line in Figure 6, left, which is a typical diffraction (Airy-like) pattern. This occurs

because the simulation has not included the finite size of the source hitherto; however, due to the incoherent nature of the X-ray source, we can convolve the obtained PSF with the gaussian angular profile of the source. If this is done, the result is the black line in Figure 6, left, which accounts for both source size and diffractive effects. The effect of assuming gaussian sources with different dimensions is shown in Figure 6, right.

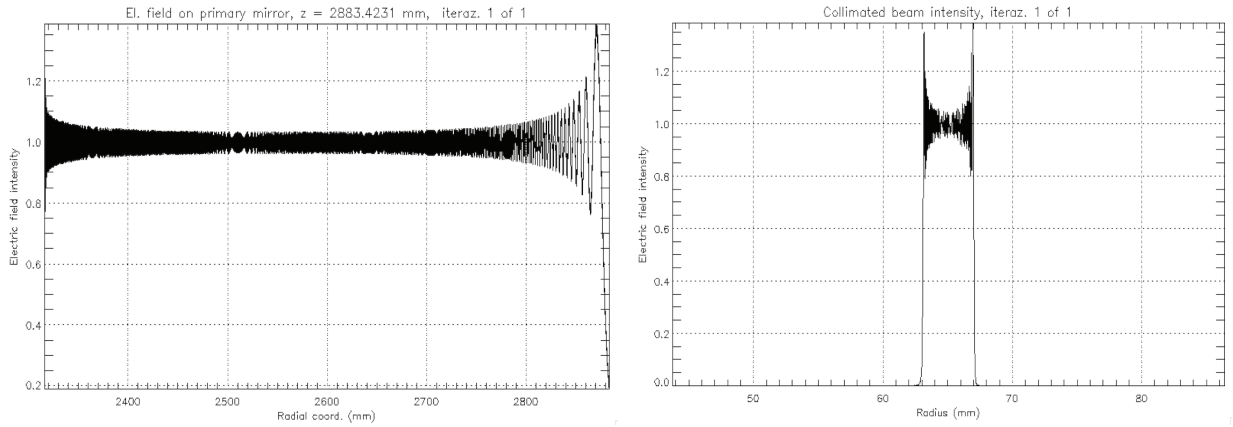

Figure 5. Left: intensity of the diffracted electric field (0.2 keV, point-like source) by the hyperbola on the parabola. Note the intensity cutoff at the illumination edge from the hyperbola, near 2900 mm. Right: intensity of the diffracted electric field at the exit of the collimator. Diffraction fringes would be completely averaged out by the incoherence of the source.

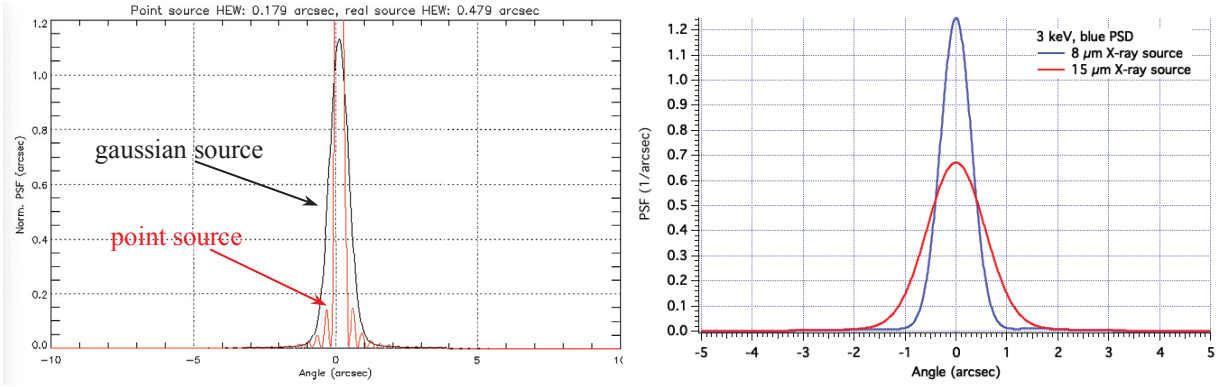

Figure 6: Left: expected PSF for a point-like source (red line) and for an 8 μm FWHM X-ray source (black line). Right: computed PSF at 3 keV for different FWHM values of the X-ray source.

We now have a PSF computation tool for assessing the effect of mirror defects of any kind. Starting now from different surface polishing PSDs (e.g., as shown in Figure 2, right), one can easily generate rough profiles compatible with that PSD and with the profile sampling frequencies (that depend on the energy and the angular size of the detection plane, as per the *sampling rules* reported elsewhere[8][13]). The rough profiles, once superimposed to the nominal Wolter-I profile, can be used to compute the diffracted field via Eqs. (2) and (4), and the expected PSF follows from the method exposed above.

The HEW computation in the tangential direction (i.e., in the plane of incidence) from the PSF is straightforward, but the result $HEW_{1D\text{-}tang}$ is only one component of the total HEW, because the X-ray source is extended in the sagittal direction also. The bi-dimensional HEW can be computed by combining the two terms as follows:

$$HEW_{2D} \approx \frac{1}{0.573}\sqrt{\frac{HEW_{1D}^2 + HEW_{1D-tang}^2}{2}} \tag{6}$$

the derivation of this result is reported in Appendix A, along with further approximations. In the next section, we apply this methodology to hypothetical polishing and figuring levels for the VERT-X mirror.

3.2. The scattering trends

We now take the 3 PSDs shown in Figure 2 and, assuming a source with an 8 μm or 15 μm FWHM, we compute the bi-dimensional HEW using the methodology explained in Sect. 3.1. The PSDs are truncated on the low-frequency side at 1 cm spatial wavelength, because defects of larger size can be considered figure defects and corrected deterministically. The HEW as a function of the X-ray energy, shown in Figure 7, encompasses the mirror roughness and the X-ray source size (15 μm and 8 μm). The two groups of curves essentially differ by an additive constant, suggesting a linear sum of the two terms. At low energies (< 4 keV) the HEW is entirely dominated by the X-ray source extent; in order to remain below 1 arcsec, it is clearly mandatory that the X-ray source be smaller than 8 μm in FWHM. As a result of the scattering, the HEW degrades with increasing energy, but the curves differ from each other. This is related to the different spectral index of the PSD in the three cases, and generally (but not always), a steeper PSD would be preferable.[14]

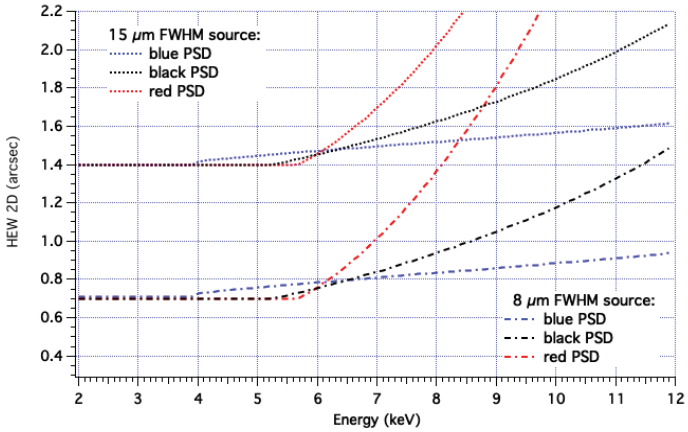

Figure 7: computed HEW values of the VERT-X collimator for increasing energies and different PSDs as in Figure 2. The small aperture diffraction term, which would appear at very low energy, is not shown here (it is in Figure 8).

The "blue" PSD is the steepest one and so it entails a much slower degradation, even if its higher content in low frequency roughness causes an earlier appearance of the scattering term. The "black" and the "red" PSDs, in contrast, exhibit a much smoother behavior and for this reason are characterized by a much faster divergence of the scattering contribution to the HEW. If the source has a 8 μm FWHM, and the VERT-X mirror finishing approaches the blue PSD, then the collimated beam will be parallel to within 1 arcsec HEW in all the energy band of interest (0.3-12 keV). The analysis does not comprise, though, the figure errors wider than 1 cm (Sect. 3.3). Neither it considers the aberrations due to misalignments between the two mirror segments (Sect. 4).

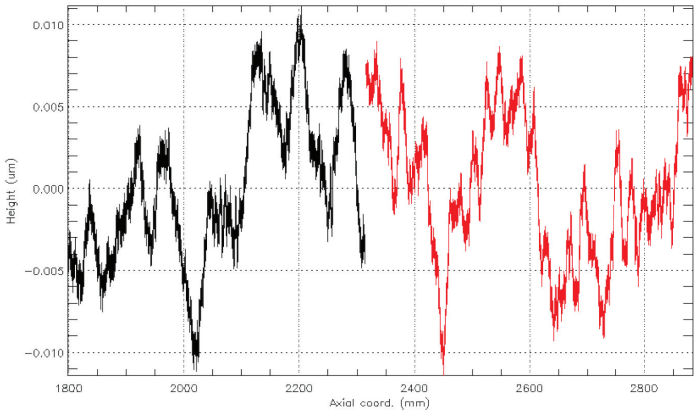

Figure 8: a synthetic profile error, generated from the superposition of harmonics with decreasing amplitudes and random phases, and a rough profile obtained from the blue PSD in Figure 2.

3.3. Accounting for figure errors

We now have a preliminary idea of the impact of roughness and of source size on the final collimation level of the VERT-X facility. In order to provide an idea of the figure error, we have elaborated (Figure 8) a possible profile, even

smoother than it would probably be necessary. The profile includes all the spatial frequencies, from the mirror length down to $(1\ \mathrm{cm})^{-1}$, with appropriately decreasing amplitudes and variable phases. Frequencies higher than $(1\ \mathrm{cm})^{-1}$ have been generated from the blue PSD in Figure 2, and superposed to the deterministic profile. The result has been processed using the Fresnel diffraction algorithm[8] for variable energies, and the relevant 2D HEW values are plotted in Figure 9.

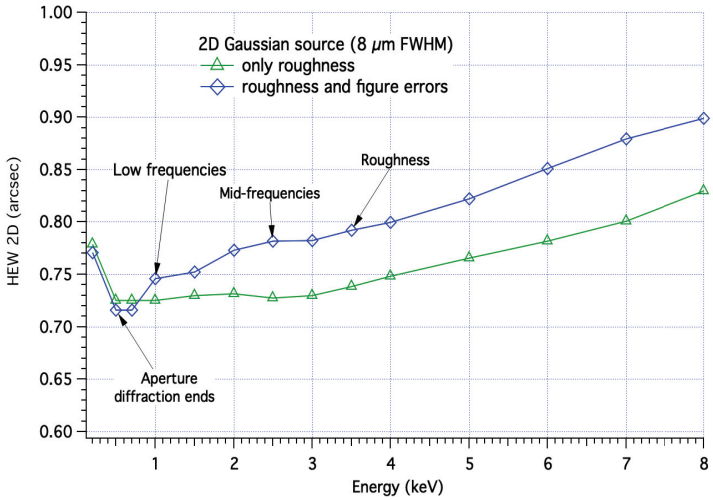

Figure 9: expected evolution of the HEW with increasing X-ray energy, using either a simple roughness model (Figure 2) or the figure + roughness profile (Figure 8).

Some relevant differences between the HEW trends shown in Figure 9 can be remarked. The one computed from roughness exhibits a plateau followed by a power of the X-ray energy. At very low energies, profile errors are not even "seen" by X-rays, leaving room only to a very small aperture diffraction term. When the complete figure error is used along with the blue PSD (Figure 2), the HEW values start to raise gradually, until stabilizing at 2.5-3 keV. Beyond this energy range the roughness effect starts to appear, quite reproducing - shifted upwards - the HEW increase due to roughness. This behavior is due to the adoption of a figure error (Figure 8) that includes a variety of spatial frequencies, not always fulfilling the smooth-surface approximation. For increasing energy, higher and higher harmonic components start to contribute to the PSF. At energies larger than 3 keV, all the figure error terms become effective and the roughness component (spatial frequencies > $(1\ \mathrm{cm})^{-1}$) begins to affect the PSF. Nevertheless, the HEW value would remain below 1 arcsec for all the energies of interest, also leaving some margin for alignment errors. This will be studied in the next section.

4. SEGMENT ALIGNMENT TOLERANCES: 2D SIMULATIONS

4.1. Theoretical background

Alignment tolerances of the parabola-to the hyperbola have been studied also. The assessment of the mutual accuracy of the two mirror segments is needed to ensure a beam collimation better than the one introduced by the source dimensions (8 μm FWHM = 0.71 arcsec), and so determine to which accuracy the parabola-hyperbola pieces have to be mutually aligned. We have investigated the sensitivity to the displacements in the six degrees of freedom, 3 translational and 3 rotational, keeping the hyperbola still and moving the parabola. The simulation was conducted using the same diffraction simulation code used in the SIMPOSIuM project[12] to simultaneously account for misalignment and diffraction (the latter will be important in UV light that will be used for the alignment process).[3] The predictions of the diffraction code were validated by means of ray-tracing also.

We have simulated the PSF of the mirror using the formula for simulating diffraction through SPO mirror modules,[11] at a generic distance D and a light wavelength λ,

$$PSF_D(\underline{r}) = \frac{1}{A_M \lambda^2 D^2} \left| \int e^{-\frac{2\pi i}{D\lambda}(\underline{r}\cdot\underline{r}_1)} e^{-\frac{\pi i}{f\lambda}\left(\frac{f}{D}-1\right)|\underline{r}_1|^2} CPF\left(\underline{r}_1\right) \mathrm{d}\underline{r}_1^2 \right|^2, \quad (7)$$

where f is the focal length, A_M is the projected mirror area, $\underline{r} = (x, y)$ are the coordinates on the focal plane, and $\underline{r}_1 = (x_1, y_1)$ are the coordinates on the I.P. of the Wolter-I mirror. The second exponential factor is responsible for defocusing when $D \neq f$, and the *complex pupil function*, CPF, is derived from the error profile $\varepsilon(\underline{r}_1)$:

$$CPF(\underline{r}_1) = \exp\left[-\frac{2\pi i}{\lambda} \cdot 2\varepsilon(\underline{r}_1) \sin\alpha\right]. \tag{8}$$

In the case being considered, no structure (ribs and membranes) of a SPO module have to be considered. Even for a perfect mirror, all we have to model is the phase change introduced by a fictitious shape error introduced by misalignments, $\varepsilon(\underline{r}_1)$. In other words, we treat the misalignment as a figure error of the parabolic segment: the error is the difference between the rotated parabola and the perfect one, projected in the plane orthogonal to the propagation direction. The resulting *optical path difference* (OPD) for two representative misalignments is shown in Figure 10. In the following subsections, we show the computation of the PSF from Eq. (7) for each species of misalignment. In order to visualize the sole effect of the misalignment, the size of the X-ray source was set to zero at this stage. For comparison, we show in Figure 11 the simulated focus of the ideal, perfectly-aligned collimating mirror in X-rays and UV light (the simulated detector has been deliberately set at different sizes for computation ease). In the UV illumination case, diffraction fringes clearly appear in the focal spot. This would hinder the observation of aberrations in UV light and set a limit the optical alignment of the two segments in an optical bench, as opposite to the position of the centroid[3] that is independent of λ and not affected by the presence of diffraction fringes.[11]

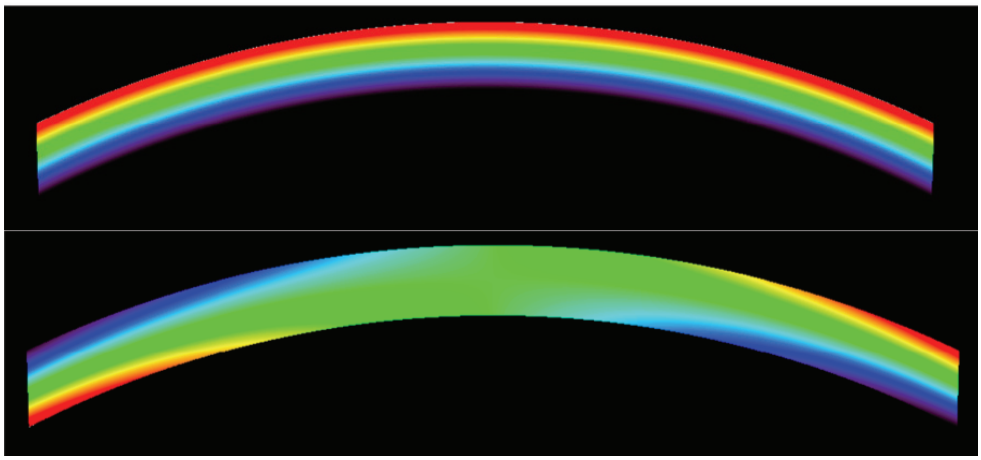

Figure 10. OPD maps (the $\varepsilon(\underline{r}_1)$ term in Eq. 8) in linear color scale, as resulting from two possible misalignments of the parabola with respect to the hyperbola. Top: misalignment in pitch. Bottom: Misalignment in yaw (see Figure 12 for the reference frame).

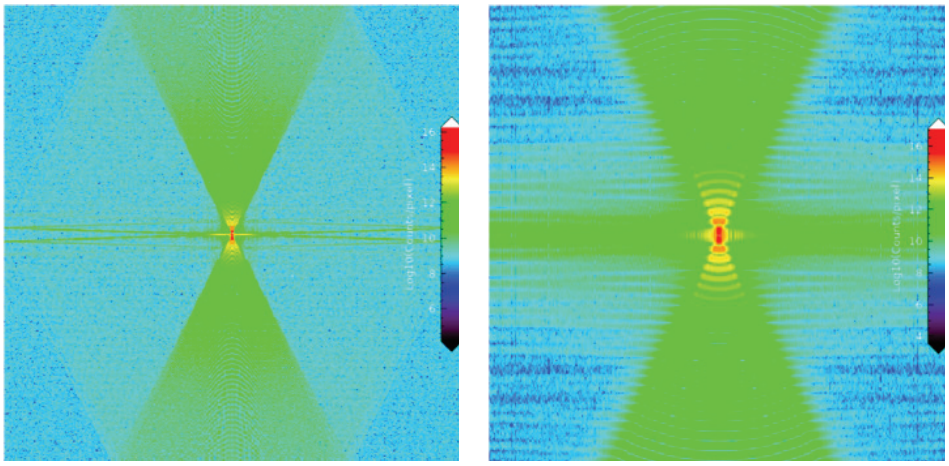

Figure 11: the focus of a perfectly aligned Wolter collimator. Left: in X-rays at 1.2 keV (λ = 1 nm), 0.5 mm wide detector. Right: in UV light, (λ =0.2 μm), 5 mm wide detector. Log color scale.

4.2. Hyperbola-Parabola rotations

The first species of parabola-hyperbola misalignments (pitch rotation) mostly affects the angle at the I.P. and is responsible for a lateral displacement in the incidence plane, that boils down to twice the rotation angle. Moreover, it causes a focal spot broadening of approximately 1 arcsec HEW for each arcsec of misalignment. The predictions of the diffraction code for this kind of misalignment are shown in Figure 13, left. Fortunately, this kind of misalignment can be almost entirely recovered by refocusing the X-ray source by just 0.82 mm (Figure 13, right). This is exactly the focal length change expected from a 0.5 arcsec variation in the incidence angle (which is half the change in the kink angle at the I.P.).

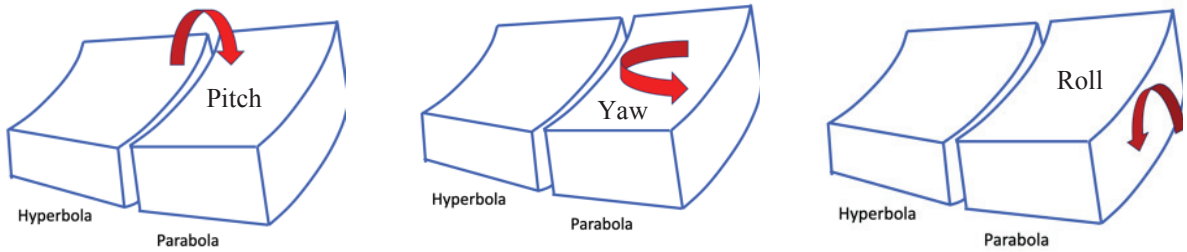

Figure 12: the three possible rotations of the parabolic segment, keeping the hyperbolic segment fixed.

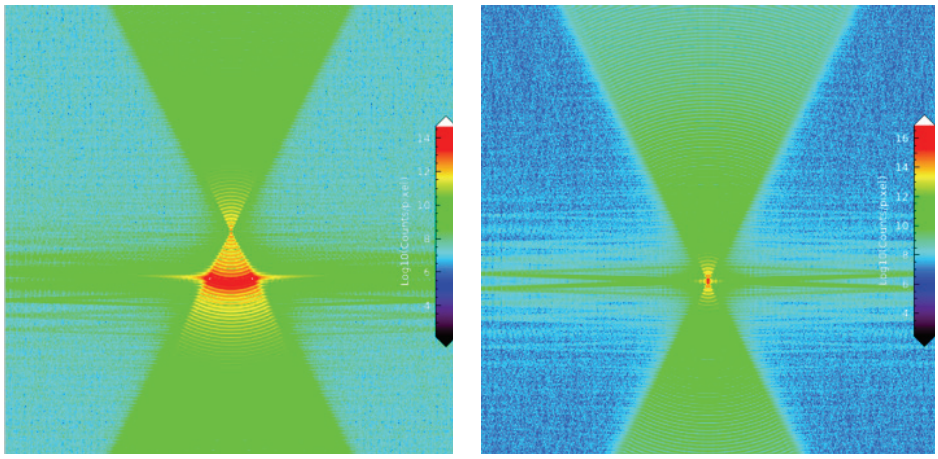

Figure 13. Left: the effect of a pitch rotation (1 arcsec) of the parabolic segment of the VERT-X mirror on the X-ray image at 1.2 keV, viewed on a detector with a 0.2 mm width, in log color scale. The lateral displacement is, as expected, near 2 arcsec, and the HEW is close to 1 arcsec. Right: after moving the focal plane 0.82 mm closer to the mirror.

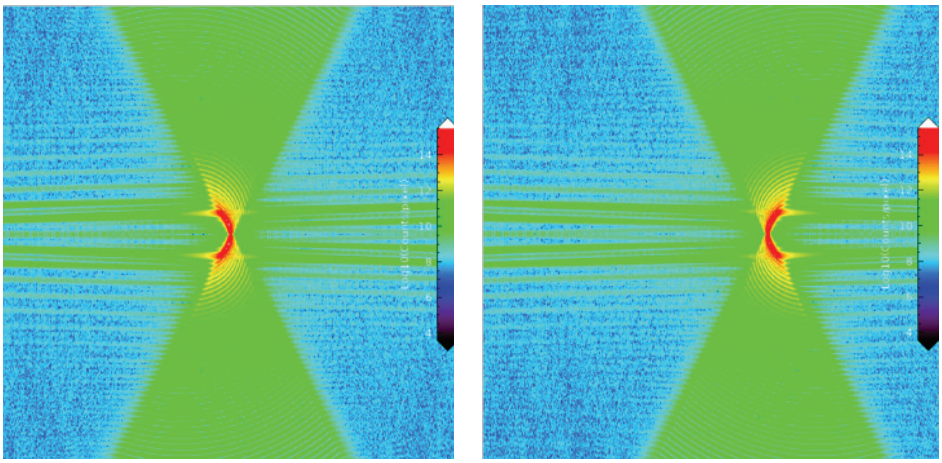

Figure 14. Left: the effect of a yaw rotation (1 arcsec) on the X-ray image at 1.2 keV, as seen on a 0.2 mm-wide detector, in log color scale. No displacement is present, as expected, and the HEW is 0.95 arcsec. Right: the effect of an 80 arcsec roll rotation.

The second kind of misalignment (yaw) causes no lateral displacement of the focal spot, only an aberration in the shape of a "C", as shown in Figure 14, left. An arcsecond rotation causes an aberration that is similar to the effect of the pitch rotation: this can be surprising at first glance, because one would expect a lesser sensitivity to rotations in yaw than in pitch. However, this would typical of optical modules having lateral apertures much smaller than the radius of curvature, as opposite to the case of the VERT-X collimator, whose azimuthal aperture is the same as the main curvature radius. Unlike pitch, a misalignment in yaw *cannot* be corrected acting on the focal plane distance.

The third kind of misalignment (roll) is responsible for both displacement and aberration (Figure 14, right). Aberration occurs in a totally similar way as for yaw rotations, but the aberration magnitude is reduced by a factor of $\tan(2\alpha)$. This species of aberration cannot be corrected by refocusing; however, the sensitivity to this rotation is so low (1 arcsec aberration for each 80 arcsec misalignment) to be easily corrected mechanically.

4.3. Hyperbola-Parabola translations

As for the translations, they are schematically depicted in Figure 15. Their impact of the focal spot degradation varies, just like in rotations. Translations of the parabolic segment along the *x*-axis yield aberrations in the usual C-shape like the one displayed in Figure 16, left. A 1 arcsec HEW is generated by a 20 μm displacement, and cannot be corrected adjusting the focal plane distance.

Translation in the *y* direction causes another "arc" aberration like the one shown in Figure 16, right. The misalignment magnitude necessary to introduce a 1 arcsec HEW aberration is the same as along the *x*-axis, but the defocusing can be, this time, mostly corrected adjusting the detector distance (Figure 17, left).

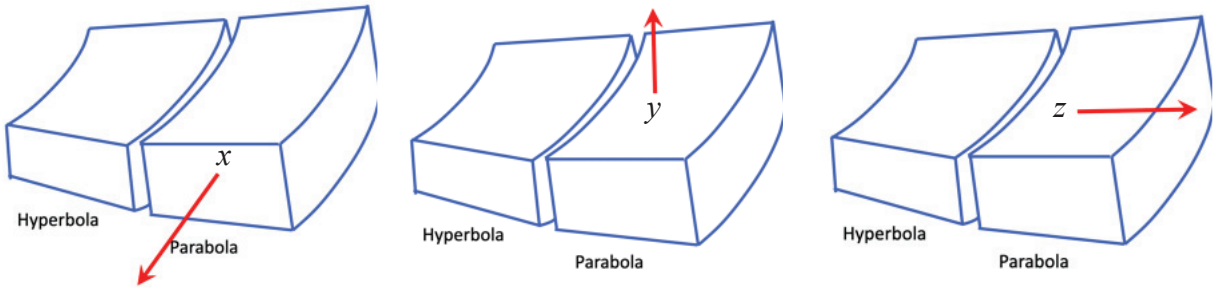

Figure 15: three translations of the parabolic segment, keeping the hyperbolic segment fixed.

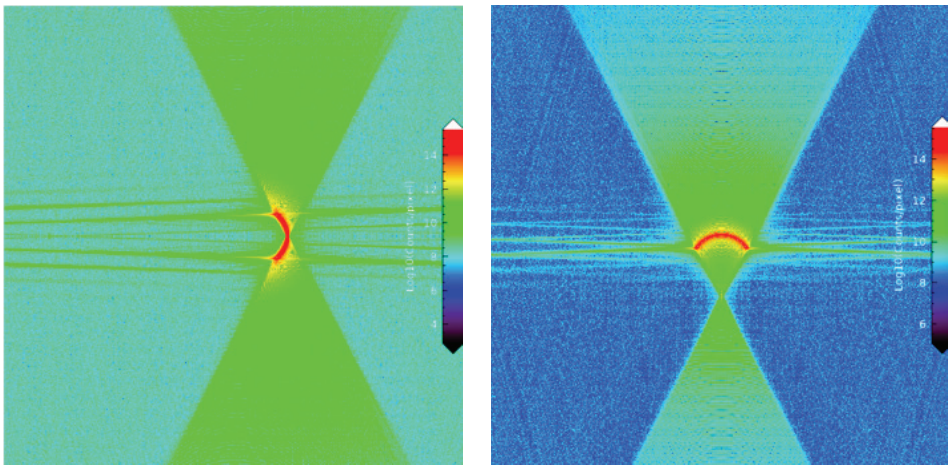

Figure 16. Left: the effect of a 20 μm translation of the parabolic segment in the VERT-X mirror along the x-axis on the X-ray image at 1.2 keV, as imaged on a 0.2 mm-wide detector. The color scale is logarithmic. The HEW is 0.93 arcsec.

Finally, the effect of misalignment along the *z*-axis, causing a totally similar defocusing as the translation along *y*, but with much lower sensitivity, is shown in Figure 17, right. This effect can be compensated also (not completely, but to a large extent) by shifting the focal plane or acting on the misalignment along *y* in the opposite direction. The simulation results are summarized in Table 1. We also indicate which misalignments can be recovered by adjusting the X-ray source distance in order to re-locate it to the best focus. This is possible only in 3 cases (R_x, T_y, T_z).

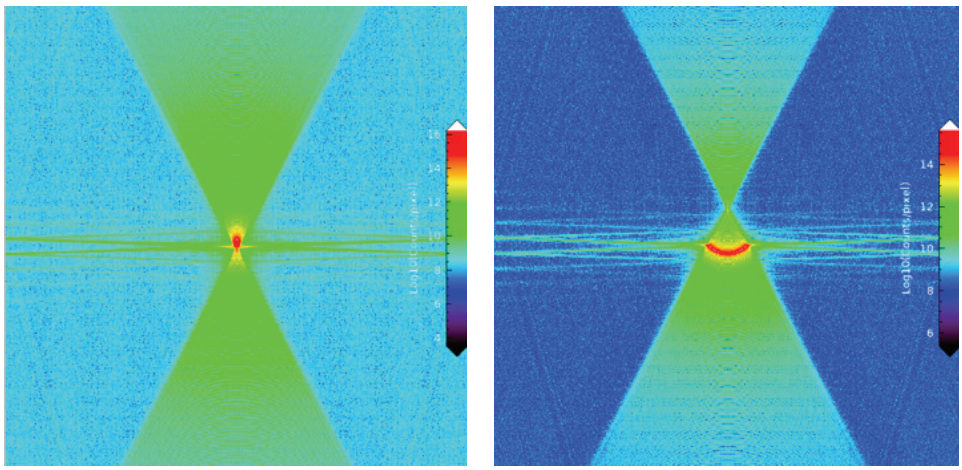

Figure 17. Left: setting the focus 0.7 mm farther to (mostly) compensate the translation along y on the X-ray image at 1.2 keV (Figure 16, right). Log color scale. Right: the defocusing effect of a 0.6 mm translation along the z-axis. The HEW is 0.94 arcsec.

Table 1: the sensitivity of the HEW to each misalignment. The magnitude of the rotation or that of the translation that degrades the HEW to 1 arcsec is listed. Also shown is the expected centroid displacement.

Misalignment type	Misalignment magnitude	Aberration HEW	HEW correct. by refocusing	Centroid Displacement
X rotation (pitch)	1 arcsec	0.9 arcsec	Yes	18 μm along Y
Y rotation (yaw)	1 arcsec	0.86 arcsec	No	1.6 μm along X
Z rotation (roll)	80 arcsec	1.0 arcsec	No	13 μm along X
X translation	22 μm	0.90 arcsec	No	13 μm along X
Y translation	20 μm	0.93 arcsec	Yes	28 μm along Y
Z translation	0.6 mm	1.0 arcsec	Yes	20 μm along Y

5. FINAL REMARKS

The VERT-X X-ray facility will be based on the collimation and expansion of an X-ray beam via a grazing incidence mirror. The collimator will be a Wolter-I profile in order to minimize aberrations resulting from small displacements of the source during the raster scan. Accurate polishing will be required and alignments of the two segments to avoid degrading the angular resolution, i.e., the divergence of the collimated beam. We have so developed software tools for predicting the expected angular resolution from a given PSD tolerance and some misalignments between the Wolter-I segments. Simulation show that the accuracy required keep the divergence on the order of 1 arcsec are demanding but feasible. Next steps will be addressed to formulate a precise error budget and a fabrication tolerance (PSD for roughness and figure errors).

APPENDIX A. HEW AND FWHM IN A GAUSSIAN FOCAL SPOT

Since 1D simulations can only be performed on 1D gaussian profiles (Sect. 3), while the specification of the source is given in terms of the 2D profile FWHM, we need to determine the relation between these parameters. The expression of a radially-symmetric, normalized 2D gaussian profile is

$$u(x,y) = \frac{1}{2\pi\sigma^2} e^{-\frac{x^2+y^2}{2\sigma^2}} = \frac{1}{2\pi\sigma^2} e^{-\frac{r^2}{2\sigma^2}}, \tag{A.1}$$

where $r^2 = x^2 + y^2$, and the corresponding 1D profile is obtained, e.g., by integration on the y-axis:

$$\int_{-\infty}^{+\infty} u(x,y)\,\mathrm{d}y = \frac{1}{\sqrt{2\pi}\sigma} e^{-\frac{x^2}{2\sigma^2}} = u(x). \tag{A.2}$$

Now, the HEW in 2D is expressed by the condition

$$\int_0^R \frac{1}{2\pi\sigma^2} e^{-\frac{r^2}{2\sigma^2}}\, 2\pi r\, \mathrm{d}r = \int_0^R \frac{2r}{2\sigma^2} e^{-\frac{r^2}{2\sigma^2}}\, \mathrm{d}r = \int_0^{\frac{R^2}{2\sigma^2}} e^{-X} \mathrm{d}X = 1 - e^{-\frac{R^2}{2\sigma^2}} = \frac{1}{2}, \tag{A.3}$$

which returns

$$HEW_{2D} = 2R = 2\sigma\sqrt{2\ln 2} = FWHM_{2D}\,; \tag{A.4}$$

this shows that in a 2D profile the HEW exactly equals the FWHM parameter. However, if a 1D gaussian profile (Eq. A.2) is considered, it is easily verified that the relation changes into

$$HEW_{1D} = 0.573\ FWHM_{2D}. \tag{A.5}$$

To a good approximation, scattering simulations[8] show that the HEW_{1D} values in the tangential direction due to the source and the one due to the scattering add up linearly:

$$HEW_{1D-tang} \approx HEW_{1D} + HEW_{scatt}. \tag{A.6}$$

In order to return to the HEW in 2D, we shall reconvert the $HEW_{1D\text{-}tang}$ into a FWHM (Eq. A.5) and recombine the latter with another HEW_{1D} in the sagittal direction, which is essentially unaffected by the scattering,

$$HEW_{2D} \approx\ FWHM_{2D}\ \approx \frac{1}{0.573}\sqrt{\frac{HEW_{1D}^2 + HEW_{1D-tang}^2}{2}}, \tag{A.7}$$

where the factor ½ under square root comes from the *orthogonality* of the two contributions. Since $HEW_{scatt} << HEW_{1D}$, then $HEW_{1D\text{-}tang}^2 \approx HEW_{1D}^2 + 2\, HEW_{1D}\, HEW_{scatt}$; hence, Eq. (A.7) can be approximated at the first order as

$$\begin{aligned} HEW_{2D} &\approx \frac{1}{0.573}\sqrt{HEW_{1D}^2 + HEW_{1D}HEW_{scatt}} = \frac{HEW_{1D}}{0.573}\sqrt{1 + \frac{HEW_{scatt}}{HEW_{1D}}} \approx \\ &\approx \frac{HEW_{1D}}{0.573}\left(1 + \frac{HEW_{scatt}}{2HEW_{1D}}\right) = \frac{HEW_{1D}}{0.573} + \frac{HEW_{scatt}}{2 \times 0.573} \approx FWHM_{2D} + HEW_{scatt}. \end{aligned} \tag{A.8}$$

ACKNOWLEDGMENTS

The VERT-X project is supported and financed by ESA.

REFERENCES

[1]. Bavdaz, M., Wille, E., Ayre, M., Ferreira, I., Shortt, B., et al., "The Athena x-ray optics development and accommodation," Proc. SPIE 11852, 1185220 (2021)

[2]. Collon, M. J., Babic, L., Barrière, N. M., Bayerle, A., Castiglione, L., et al., "X-ray mirror development and production for the Athena telescope," Proc. SPIE 11852, 118521Z (2021)

[3]. Valsecchi, G., Bianucci, G., Marioni, F., Vernani, D., Zocchi, F., Korhonen, T., Pasanen, M., Pareschi, G., Ferreira, F., Bavdaz, M., Wille, E., Doyle, D., "Facility for alignment, assembly, and integration of the SPO mirror modules onto the ATHENA telescope," Proc. SPIE 11822 (2021)

[4]. Bradshaw, M., Burwitz, V., Hartner, G., Langmeier, A., Vacanti, G., et al., "Testing ATHENA optics: a new measurement standard at the PANTER x-ray test facility," Proc. SPIE 11852, 1185223 (2021)

[5]. Moretti, A., Pareschi, G., Uslenghi, M., Tordi, M., Bressan, R., Valsecchi, G., Zocchi, F., Attinà, P., Amisano, F., Sironi, G., Salmaso, B., Basso, S., Tagliaferri, G., Spiga, D., La Palombara, N., Fiorini, M., Dury, F., Marioni, F., Parissenti, G., Parodi, G., Wille, E., Corradi, P., Bavdaz, M., Ferreira, I., "VERT-X: VERTical X-ray raster-scan facility for ATHENA calibration. The concept design," Proc. SPIE 11119, 111190O (2019)

[6]. Moretti, A., Spiga, D., Sironi, G., Pareschi, G., Basso, S. Tagliaferri, G., Valsecchi, G., Zocchi, F., Vernani, D., Marioni, F., Tordi, M., De Lorenzi, S., Parodi, G., Amisano, F., Corradi, P., Ottolini, M., Ferreira, I., Bavdaz, M., Parissenti, G., La Palombara, N., Uslenghi, M., Civitani, M, Ghigo, M., "The VERT-X calibration facility: development of the most critical parts," Proc. SPIE 11822, 118220K (2021)

[7]. Spiga, D., Raimondi, L., "X-ray optical systems: from metrology to Point Spread Function," Proc. SPIE 9209, 92090E (2014)
[8]. Raimondi, L., Spiga, D., "Mirrors for X-ray telescopes: Fresnel diffraction-based computation of point spread functions from metrology," A&A 573, A22 (2015)
[9]. Salmaso, B., Basso, S., Cotroneo, V., Ghigo, M., Pareschi, G., Redaelli, E., Sironi, G., Spiga, D., Tagliaferri, G., Vecchi, G., Fiorini, M., Incorvaia, S., Uslenghi, M., Paoletti, L., Ferrari, C., Zappettini, A., Lolli, R., Sanchez del Rio, M., Burwitz, V., Christensen, F., Della Monica Ferreira, D., Gellert, N., Massahi, S., Bavdaz, M., Ferreira, I., "Building the BEaTriX facility for the ATHENA mirror modules X-ray testing," Proc. SPIE 11822, 118220M (2021)
[10]. Vecchi, G., Cotroneo, V., Ghigo, M., Basso, S., Salmaso, B., Sironi, G., Spiga, D., Conconi, P., Pareschi, G., Tagliaferri, G., Burwitz, V., Hartner, G., Müller, T., Rukdee, S., Schmidt, T., Christensen, F., Della Monica Ferreira, D., Gellert, N., Massahi, S., Bavdaz, M., Ferreira, I., "Manufacturing and testing of the X-ray collimating mirror for the BEaTriX facility", Proc. SPIE 11822, 118220N (2021)
[11]. Spiga, D., Della Monica Ferreira, D., Shortt, B., Bavdaz, M., Bergbäck Knudsen, E., Bianucci, G., Christensen, F., Civitani, M., Collon, M., Conconi, P., Fransen, S., et al., "Optical simulations for design, alignment, and performance prediction of silicon pore optics for the ATHENA x-ray telescope," Proc. SPIE 10399, 103990H (2017)
[12]. Sironi, G., Spiga, D., Moretti, A., Pareschi, G., Tagliaferri, G., Della Monica Ferreira, D., Bergbäck Knudsen, E., S Jegers, A., Ferreira, I., Bavdaz, M., "Open-source simulator for ATHENA X-ray telescope optics," Proc. SPIE 11822, 118220I (2021)
[13]. Spiga, D., Cocco, D., Hardin, C. L., Morton, D. S., Ng, M. L., "Simulating the optical performances of the LCLS bendable mirrors using a 2D physical optics approach," Proc. SPIE 10761, 1076107 (2018)
[14]. Spiga, D., "Analytical evaluation of the X-ray scattering contribution to imaging degradation in grazing-incidence X-ray telescopes," A&A, Vol. 468, n. 2 pp. 775-784 (2007)